coatings

MDPI

Article

Diffusion Aluminide Coatings for Hot Corrosion and Oxidation Protection of Nickel-Based Superalloys: Effect of Fluoride-Based Activator Salts

Virgilio Genova, Laura Paglia, Giovanni Pulci, Cecilia Bartuli * and Francesco Marra

Department of Chemical Engineering, Materials, Environment, University of Rome "La Sapienza"—INSTM Reference Laboratory for Engineering of Surface Treatments, Via Eudossiana, 18-00185 Rome, Italy; virgilio.genova@uniroma1.it (V.G.); laura.paglia@uniroma1.it (L.P.); giovanni.pulci@uniroma1.it (G.P.); francesco.marra@uniroma1.it (F.M.)

* Correspondence: cecilia.bartuli@uniroma1.it; Tel.: +39-06-44585633

Abstract: The influence of two different fluoride-based activator salts (NH_4F and AlF_3) was studied for diffusion aluminide coatings obtained via pack cementation on a Ni-based superalloy (René 108DS). The resistance to oxidation and hot corrosion was assessed as a function of the concentration of activator salts used during the synthesis process by means of pack cementation. Two different concentrations were selected for activator salts (respecting the equimolarity of fluoride in the synthesis) and the obtained diffusion coatings were compared in terms of morphology, thickness and composition, as well as in terms of microstructural evolution after high temperature exposure. Isothermal oxidation tests were conducted at 1050 °C in air for 100 h in a tubular furnace. The oxidation kinetics were evaluated by measuring the weight variation with exposure time. The microstructural evolution induced by the high temperature exposure was investigated by SEM microscopy, EDS analysis and X-ray diffraction. Results showed that the coatings obtained with AlF_3 activator salt are thicker than those obtained using NH_4F as a consequence of different growth mechanism during pack-cementation. Despite this evidence, it was found that the NH_4F coatings show a better oxidation resistance, both in terms of total mass gain and of quality of the microstructure of the thermally grown oxide. On the other hand, coatings produced with high concentration of AlF_3 exhibited a better resistance in hot corrosion conditions, showing negligible mass variations after 200 h of high temperature exposure to aggressive NaCl and Na_2SO_4 salts.

Keywords: diffusion aluminide; gas turbines; hot corrosion; isothermal oxidation; activator salt; superalloys

Citation: Genova, V.; Paglia, L.; Pulci, G.; Bartuli, C.; Marra, F. Diffusion Aluminide Coatings for Hot Corrosion and Oxidation Protection of Nickel-Based Superalloys: Effect of Fluoride-Based Activator Salts. *Coatings* **2021**, *11*, 412. https://doi.org/10.3390/coatings11040412

Academic Editor: Ingrid Milošev

Received: 15 March 2021
Accepted: 30 March 2021
Published: 1 April 2021

1. Introduction

Materials used in hot sections of aero- and land-based gas turbines are designed to endure severe operating conditions and must be able to resist both hot corrosion and high temperature oxidation. Nickel-based superalloys are usually employed in high temperature sections of the engine, whereas TiAl components have aroused great interest in recent decades for the less thermally stressed areas [1–3]. A great scientific and technological interest is thus devoted to thermal barrier coatings (TBCs) [4–9] as heat resistant surface layers deposited on metallic components of gas turbine engines (usually made of Ni- or Co-based superalloys), allowing for efficient protection from high temperature inlet gases and therefore providing improved engine performance.

A typical TBC system consists of a diffusion coating or a *M*CrAlY bond coat (where *M* is Co and/or Ni), providing the chemical resistance, and a ceramic topcoat (most often made of yttria partially stabilized zirconia, YSZ) acting as thermal barrier [10–12].

Diffusion aluminide coatings are produced by high temperature chemical processes where aluminium diffuses through the surface of the superalloy and reacts to form nickel

aluminide surface layers. At high operating temperatures, the Al present in the NiAl layer is preferentially oxidized and forms a thin and dense alumina scale, acting as a diffusion barrier and reducing the oxidation rate of the substrate.

Diffusion coatings can be produced by several methods, mainly pack cementation processes (including slurry and above-the-pack processes) and chemical vapour deposition (CVD) [13–15].

Pack cementation is essentially an in situ chemical vapour deposition process. One of the steps, which is common with CVD processes, is the generation of vapours containing aluminium, or other metallic constituents of the coating. The key step is the formation of a volatile aluminium sub-halide, AlX_n (X = F, Cl, Br; $n < 3$), which occurs at a temperature higher than 800 °C. This species reacts with the surface of the Ni alloy, depositing aluminium by the following reaction:

$$AlX_n + Ni \rightarrow AlNi_y + AlX_3 \quad (1)$$

The difference between pack and CVD processes lies in the mechanism by which AlX_n is generated and transported.

The intermetallic layer created at the surface has the composition $NiAl_y$ ($3 \geq y \geq 1/3$). While aluminium is brought to the surface by a vapour-phase process, its diffusion into the surface is a solid-state process. The vapours are carried onto the specimen surface and react with the alloy elements, forming a coating composed of intermetallic phases.

For pack aluminizing, the component to be coated is previously cleaned, dried and then placed in an air-tight reactor containing a mixture of aluminium (or aluminium alloy) powder, a halide activator (e.g., NH_4Cl), which reacts with aluminium to generate the aluminium halide vapours, and inert Al_2O_3 fillers, added to prevent the sintering of Al-based pellets.

Levine and Caves [16] demonstrated that fluoride salts are more efficient activators than other halides for Al deposition, despite the dangerous vapour by-products generated by the reaction.

The formation of AlF_x in the vapour phase is a fundamental step of the diffusion coating growth mechanism, suggesting that the use of metallic fluoride directly as an activating salt could lead to a higher yield in the coating deposition. However, while this hypothesis appears plausible and convincing, no experimental data are presently available in the literature comparing different fluorides, with and without aluminium, in terms of quality and performance of the produced coatings.

To offer a contribution to filling this experimental gap, in the present paper a comparative investigation was carried out using two different fluorides as activators: ammonium fluoride, NH_4F, (used conventionally in pack cementation) and aluminium fluoride, AlF_3.

Ammonium fluoride, as reported elsewhere [17], is the perfect candidate as an activator salt, because of its thermal decomposition, occurring in the temperature range between 100 and 120 °C according to the following reaction:

$$NH_4F_{(crystalline)} \rightarrow NH_{3\,(gas)} + HF_{(gas)} \quad (2)$$

The hydrofluoric acid produced by reaction (2) reacts with solid packs to obtain the vapour phase of aluminium fluoride.

In the case of AlF_3, the thermal decomposition occurs by several consequent reactions, taking place at different temperatures. As a consequence of the hydrolysis of AlF_3, HF is formed together with gaseous HF-AlF complexes. The formation of these complexes is strongly dependent on the temperature, and the process of hydrolysis can be divided into three temperature-dependent steps. The first step (up to 250 °C) is characterized by water loss absorbed in the crystal lattice of the aluminum fluoride and the continuous formation of HF. In the second temperature range (250–550 °C) the formation of H-AlF_4 can be observed. The final result of the hydrolysis is a higher vapour concentration of $AlFx$ inside the vessel reactor than the ammonium case [18].

The higher partial pressure could theoretically be responsible for a higher reaction yield and, therefore, should allow one to obtain the same number of products using a lower amount of reactants. A second advantage of the use of AlF_3 as a reactive salt would consist in the formation of lower amounts of by-products in the exhaust gases, i.e., gaseous halides, polluting and of difficult disposal. In fact, the treatment of reaction products certainly represents one of the major drawbacks of the use of fluorides as activating salts in the pack cementation process.

The aim of this work is to investigate the difference, in terms of coating microstructure, oxidation, and hot corrosion resistance, of two types of diffusion aluminide coatings, characterized by analogous composition but obtained by the two different precursors, replicated for different salt concentrations.

2. Experimental

2.1. Coatings Deposition

The substrates used for the present investigation are made by a directionally solidified nickel-based superalloy, commercially known as René 108DS, whose composition is shown in Table 1. A Ni-base superalloy cylindrical rod was cut in discs (19.2 mm diameter, 6 mm thickness), cleaned with acetone, and polished with a P400 mesh SiC paper; the samples were then rinsed in acetone by an ultrasonic bath in order to remove any abrasive residues of polishing and the surface roughness was evaluated by a Talyscan 150 (Taylor Hobson, Leicester, UK) in order to guarantee the same surface finish for the aluminizing process [19]. The measured average roughness Ra was 0.09 ± 0.01 µm for each substrate.

Table 1. Chemical composition (weight %) of directionally solidified René 108DS nickel-base superalloy.

Alloy	Ni	Cr	Co	Al	Ti	Mo	W	Hf	Ta
René 108 DS	Bal.	8.4	9.5	5.5	0.7	0.5	9.5	1.5	3.0

Diffusion aluminide coatings were produced by a semi-sealed high temperature-low activity (HTLA) [20] pack cementation process, in the configuration "above-the-pack". In this last arrangement, the samples to be coated are positioned on a grid, placed "above" the packs tank under inert Ar atmosphere. This allows the vapour phase, containing the metal to be deposited, to get in contact with the surface of the sample while avoiding direct contact between the reagent powders and the component to be coated, preventing the accidental direct sintering of the powders on the substrate and promoting the formation of a cleaner coating.

The HTLA mechanism, as reported in many publications [21–25], generates an outward growth of the coating, since the diffusion rate of Ni is higher than that of Al at temperatures higher than 800 °C.

The temperature profile followed in the four subsequent steps of the deposition process is reported in Table 2. In particular, steps 2 and 3 consist of the thermal decomposition of the NH_4F and the vapour-phase formation of sub-stoichiometric AlF_x, respectively, while the actual diffusion of aluminium takes place during the longer (8 h) high temperature exposure in step 4 [26]. All pack cementation coatings were obtained in the same time and temperature deposition conditions.

The activator salt powders (NH_4F and AlF_3, Sigma-Aldrich Italia, Milan, Italy, both with purities ≥99.99%) were dried in furnace at 80 °C before deposition. To investigate the quantitative effect of activator salts in the formation of the coating, two different concentrations were used for each salt. In Table 3, the concentrations in terms of wt.% of the pack alloy and mole of fluoride are reported for NH_4F- and AlF_3-activated diffusion coatings. For all depositions, the equimolarity of fluoride was respected. An Al-Cr (70 wt.% in Al) master alloy was used as an aluminium precursor in the form of pellets, as reported elsewhere [27].

Table 2. Temperature profile used in the four steps of the high temperature-low activity HTLA above-the-pack cementation deposition.

Step	Temperature (°C)	Time (h)	Note
1	100	0.5	Water traces removal
2	150	1	Thermal decomposition of NH_4F [14]
3	600	2	Formation of AlF*x*-g
4	1000	8	Diffusion of Al

Table 3. Concentration of activator salts with respect to Al packing alloy for the different diffusion coatings.

Coating Name	Activator Salt Type	Activator Salt Concentration (wt.%)	Moles of Activator Salt
NF1	NH_4F	0.050	0.0135
AlF1	AlF_3	0.100	0.0135
NF2	NH_4F	0.075	0.0202
AlF2	AlF_3	0.170	0.0202

2.2. Isothermal Oxidation and Hot Corrosion Tests

Isothermal oxidation tests of the aluminide coatings were carried out at 1050 °C in a tubular furnace, in air. The specimens were gradually introduced in the furnace hot section in order to avoid any thermal shock effect. For each cycle (lasting 7 or 14 h), the specimens were removed from the furnace and cooled in air to room temperature in a dryer with silica gel desiccant, to avoid water adsorption during the cooling phase. The mass variation (either positive or negative), that occur as a consequence of the formation of the oxide scale or of its detachment, was measured after every cycle using a Mettler Toledo (Mettler-Toledo S.p.A., Milan, Italy) analytical balance with a resolution of 0.0001 g. Four samples were tested for each type of coating, and the average value of mass variation was reported.

Hot corrosion tests were carried out at 900 °C [28–30] in a high-temperature furnace equipped with a fume hood (Forni De Marco, Roma, Italy). The corrosive slurry was prepared by mixing NaCl and Na_2SO_4 powders in the weight ratio of 1/3 [31], and adding dropwise to the salt mixture the minimum amount of water as to obtain the suitable viscosity for the complete and uniform covering of the samples surface. The slurry deposited on the samples was dried on a heating plate before heat treatment. The amount of dried corrosion slurry added for every hot corrosion cycle was 2 mg/cm^2.

After every hot corrosion cycle (10 h of high temperature exposure), the specimens were washed in hot distilled water to remove the unreacted salts and soluble corrosion products before measuring mass variations.

2.3. Coatings Characterization

Microstructural analysis of aluminized surfaces was performed by a Philips XL-40 scanning electron microscope (FEI B.V, Eindhoven, The Netherlands) to investigate the microstructure of the obtained intermetallic coatings. Samples were prepared for SEM analysis by mounting in epoxy resin and polishing with a sequence of P400, P600, P800 and P1200 mesh SiC papers and diamond suspensions from 9 down to 1 μm (PRESI Mecatech P 120 Polishing Machine, Presi SA, Grenoble, France).

Elemental analysis was performed by energy dispersive spectroscopy and elaborated with the TEAM software (EDAX Octane SSD, Ametek Inc., Berwyn, PA, USA), before and after oxidation and hot corrosion tests.

X-ray diffraction (XRD) analysis was performed with a Philips X'Pert device (PANalytical B.V., Almelo, The Netherlands) on the as exposed samples (before washing) to investigate the phase structure evolution of the coatings after isothermal oxidation and hot corrosion tests. The XRD device operated at 40 KV and 40 mA with CuKα_1 radiation ($\lambda_{K\alpha1}$ = 1.540598 Å, $\lambda_{K\alpha2}$ = 1.544426 Å), a scan range of 15°–85° (2θ), a step size of 0.02° and counting time of 2 s.

3. Results and Discussion

3.1. Surface Microstructure of AS-Deposited Aluminide Coatings

The surfaces of two aluminide coatings obtained with the two activator salts are shown in Figure 1. The polyhedral structure is typical of diffusion aluminide coatings, and consists of polygonal grains surrounded by a continuous network of β-NiAl phase, as also observed in the literature [32,33]. No significant differences can be observed in the microstructure of the two coatings: the polyhedral frame appears regular in both cases, with a size in the range of 25–60 μm for NH_4F activator and in the range of 15–40 μm for AlF salt.

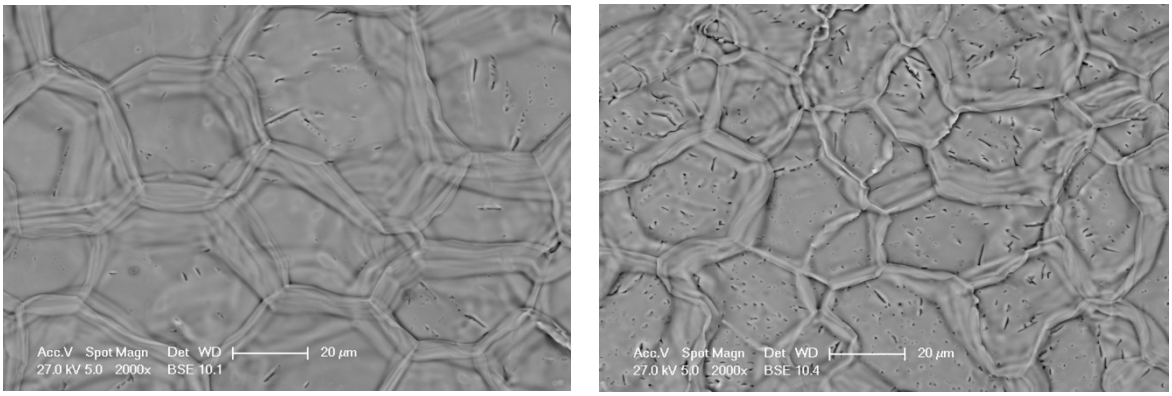

(**a**) (**b**)

Figure 1. SEM micrographs of the top surface of samples NF1 (**a**) and AlF2 (**b**), evidencing a polyhedral structure typical of diffusion aluminide coatings, consisting of polygonal grains surrounded by a continuous network of β-NiAl phase.

X ray diffraction analysis shows that β-NiAl is the only phase formed on the samples treated by NH_4F activated pack-cementation. The comparison of XRD patterns for the sample NF1 and AlF2 after aluminization is reported in Figure 2. The pattern of the NF1 sample shows the presence of only two diffraction NiAl peaks (corresponding to planes 111 and, with lower intensity, 110), thus demonstrating that the growth of intermetallic layer is highly oriented, as a consequence of the directional solidification of the nickel-based superalloy: the morphology of diffusion aluminide coatings obtained by pack-cementation appears in fact to be strongly influenced by the crystallographic orientation of the substrate surface. On the contrary, the XRD pattern of the AlF2 sample is shifted in comparison with the NF1 pattern and it matches with the Al-rich phase $Ni_{0.9}Al_{1.1}$ (JCPDS No. 441187). This could be the result of a non-completed diffusion of the Al during the pack cementation process due to the higher vapour phase concentration [34] induced by the thermal decomposition mechanism of the AlF_3.

EDS elemental profiles evaluated along the cross-section of the as coated samples are reported in Figure 3. In the NF1 sample (Figure 3a) the pack cementation process led to the formation of a continuous layer with a Ni and Al concentrations consistent with the presence of β-NiAl phase. On the contrary, the AlF2 sample (Figure 3b) exhibits an Al-rich eternal layer and an irregular profile of concentration.

In HTLA pack cementation, aluminium is deposited on the surface while nickel diffuses outward from the substrate to the surface [35]. A β-NiAl surface layer is thus formed. The elements characterized by slower diffusion rates are, in fact, unable to form significant concentration levels in the outwardly growing β-NiAl. The low solubility of heavier elements composing the superalloy in the β-NiAl phase produces precipitates in a specific intermediate area called interdiffusion zone (IDZ) [20].

The cross-section SEM micrographs reported in Figure 4 for samples NF1 (Figure 4a) and AlF2 (Figure 4b) show the typical aspect of the diffusion aluminide coating. All the coatings consist of two layers, i.e., the single phase (β-NiAl) bond coat, that does not contain precipitates, and the IDZ, characterized by the presence of precipitates from

heavier elements of the superalloy. The thickness of the β-NiAl layer and of the IDZ for all investigated samples, as measured from SEM cross-section images, are resumed in Table 4. The results show that, despite identical deposition procedures, using AlF_3 as an activator salt leads to formation of thicker β-NiAl and IDZ layers, with an increase of about 20% for the lower number of activator moles and almost 50% for the highest amount of salt.

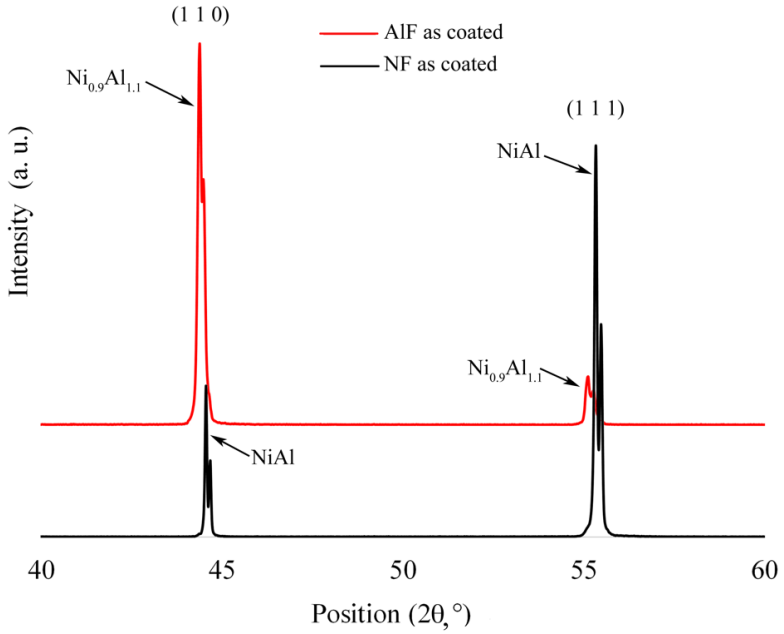

Figure 2. XRD patterns of the sample NF1 and AlF2, evidencing the presence of oriented β-NiAl phase for the NF1sample and the Al-rich β-NiAl for the AlF2 sample.

Table 4. Microstructural features of the diffusion coatings obtained using NH_4F and AlF_3 as activator salts: thickness of the β-NiAl layer and of the Interdiffusion Zone (IDZ).

Sample Name	β-NiAl Thickness (μm)	IDZ Thickness (μm)
NF1	23 ± 1.0	20 ± 0.9
AlF1	27 ± 1.2	24 ± 0.9
NF2	20 ± 0.6	19 ± 0.7
AlF2	30 ± 0.9	25 ± 0.8

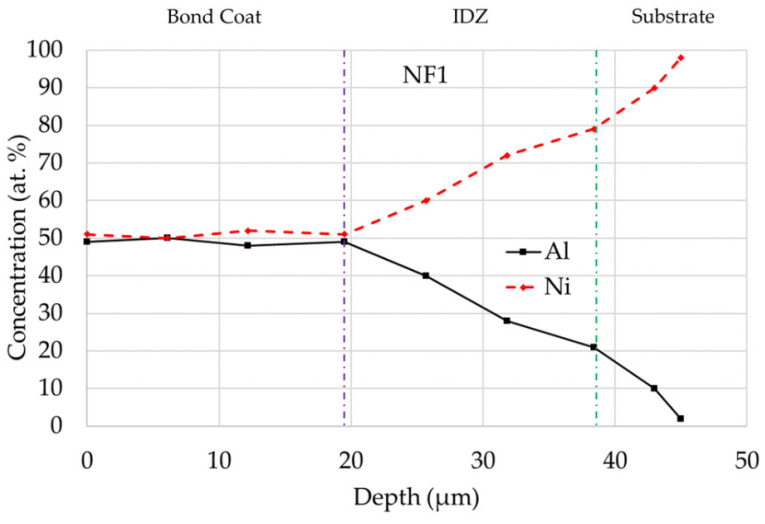

(**a**)

Figure 3. *Cont.*

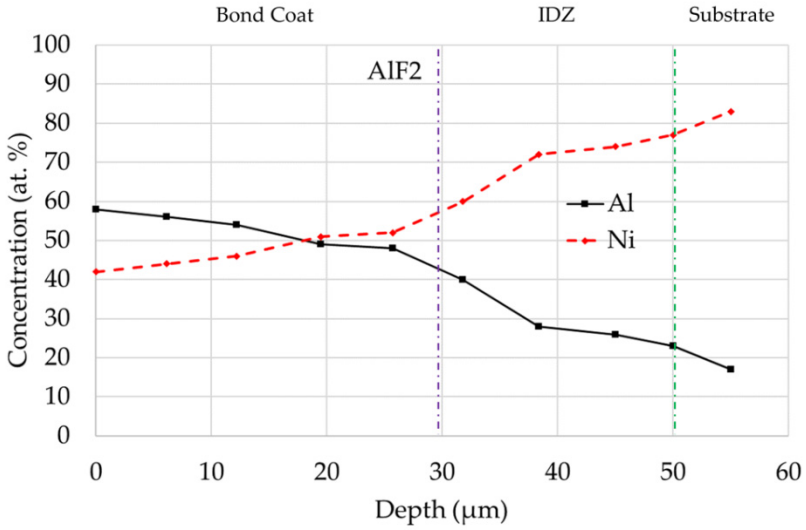

(**b**)

Figure 3. EDS linear analysis on the cross-section for the NF1 sample (**a**) and AlF2 sample (**b**). In the EDS quantitative analysis is reported only the Ni and Al.

This evidence can be explained by considering the different quantities of aluminium made available on the surface of the superalloy as the diffusion progresses. In fact, ammonium fluoride decomposes in a temperature range of 100–120 °C and forms ammonia and fluoridric acid, while in the case of aluminium fluoride, as a result of a hydrolysis reaction, not only HF, but also gaseous Al and F compounds are formed [18]. Therefore, only in the case of AlF_3, aluminium in the vapour phase atmosphere can derive both from the packs and from the activator salts. Yamai and Saito [36] showed that AlF_3 hydrolyzes in presence of water traces generating gaseous compounds according to the reaction:

$$AlF_{3(s)} + 3H_2O_{(v)} \rightarrow AlOF_{(g)} + 2HF_{(g)} \quad (3)$$

The AlOF (aluminium oxyfluorides) is an intermediate gaseous compound stable even at high temperatures, and could play an important role in the Al-containing vapour phase diffusion [37].

3.2. Comparison of Oxidation and Hot Corrosion Kinetics

The oxidation and hot corrosion kinetics were evaluated by considering the average weight gain as a function of exposure time. A standard deviation of about ±20% was calculated for the weight variation at each exposure time (error bars were not reported in the graph for better readability).

The isothermal oxidation curves are reported in Figure 5. Exposure of aluminide coatings causes the selective oxidation of β-NiAl, which forms a protective Al_2O_3 scale. For all investigated samples, experimental data fitting confirmed the parabolic trend of oxidation kinetics, according to Monceau's parabolic model (Figure 5—dashed lines) [38].

The comparison of the XRD patterns registered at 0, 25, 50, 75 and 100 h of oxidation time shows that the characteristic peak of the β-NiAl shifts towards higher angles for increasing time of exposure (Figure 6). This can be explained considering the variation of the aluminium concentration in the crystal lattice with consequent variation of the cell parameters. The selective oxidation of the intermetallic coating to Al_2O_3 leads to the depletion of Al inside the bond coat. As a consequence, an increase in the concentration of the Ni within the intermetallic layer can be observed, with relative decrease in the cell parameter, *a*, thus producing a shift of the peaks towards higher angles [39].

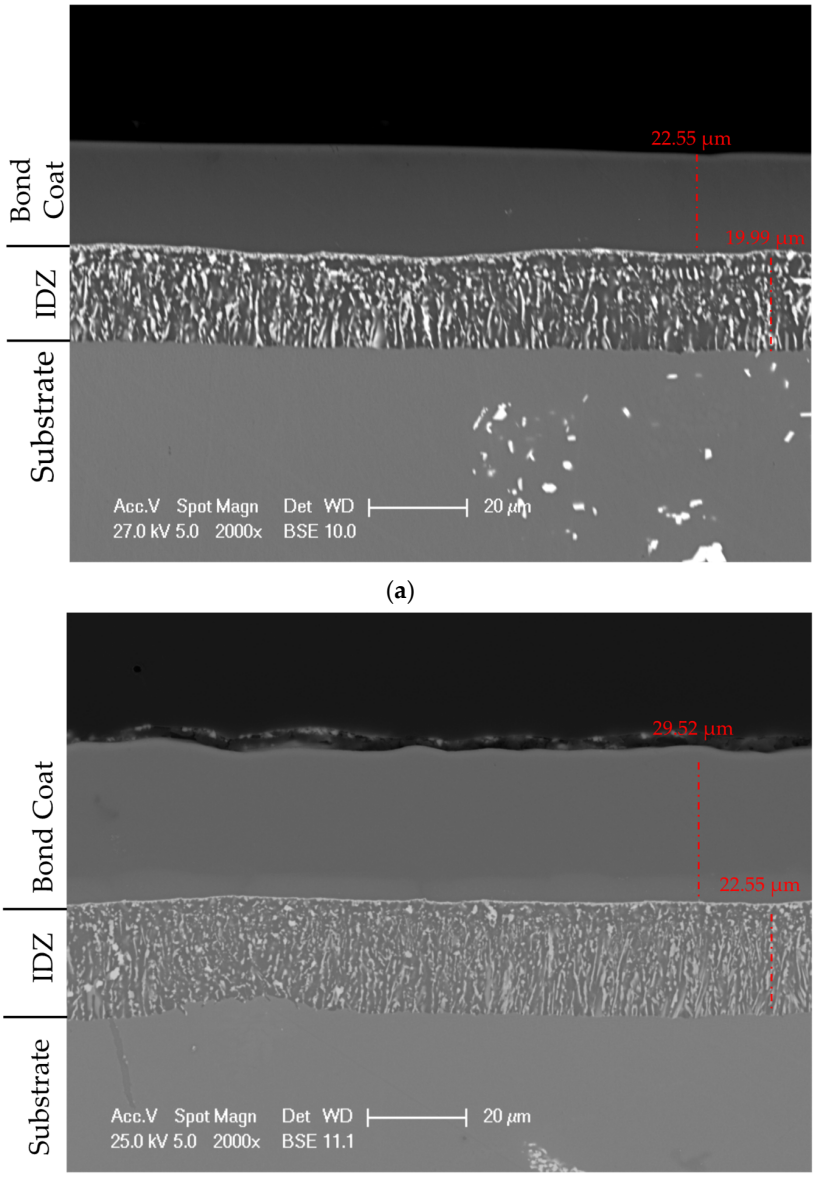

Figure 4. Cross-section SEM micrographs of samples NF1 (**a**) and AlF2 (**b**).

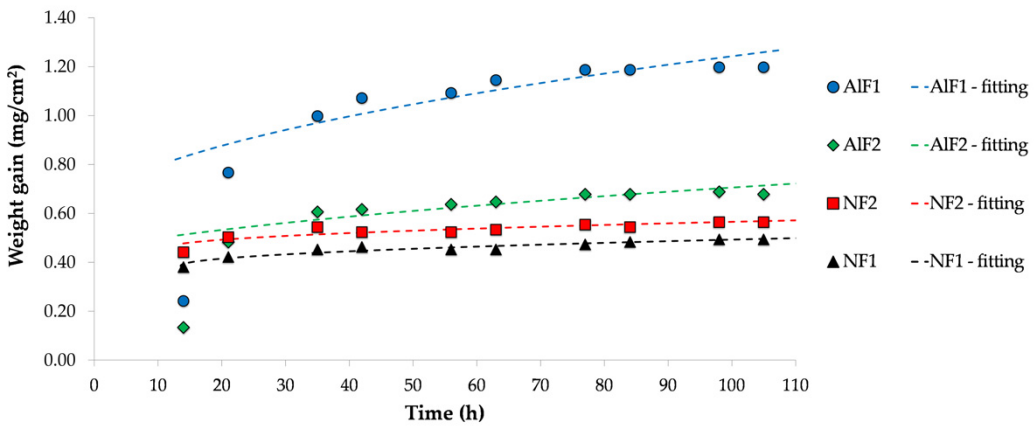

Figure 5. Isothermal oxidation kinetics (weight gain vs time) at 1050 °C for NF and AlF samples. Dashed lines are referred to the data fitting with a parabolic model

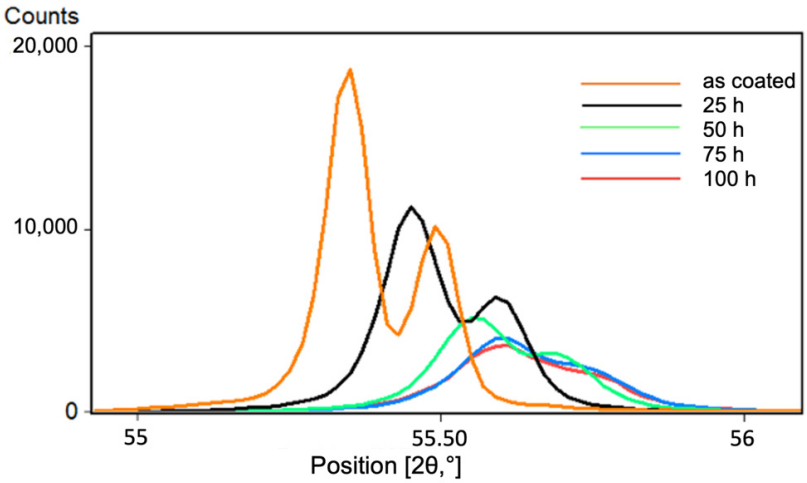

Figure 6. Evolution of the position of the characteristic (111) diffraction peak of β-NiAl with oxidation time (25, 50, 75, 100 h).

Despite the differences in thickness of the β-NiAl zone in AlF_3 and NH_4F samples, the oxidation kinetics exhibit similar trends for all the coated specimens, as observed in Figure 5. Samples protected by diffusion coatings never attain the spalling of the oxide layer. However, NF samples attain earlier the weight gain plateau and show the best oxidation resistance behaviour in terms of total mass gain after 100 h.

In Figures 7 and 8 the SEM cross-section images of representative samples are shown after 100 h of oxidation at 1050 °C. Please note that the detachment of the surface oxide layers (Figure 8) is an artefact produced during the metallographic preparation of the samples (cutting, grinding and polishing).

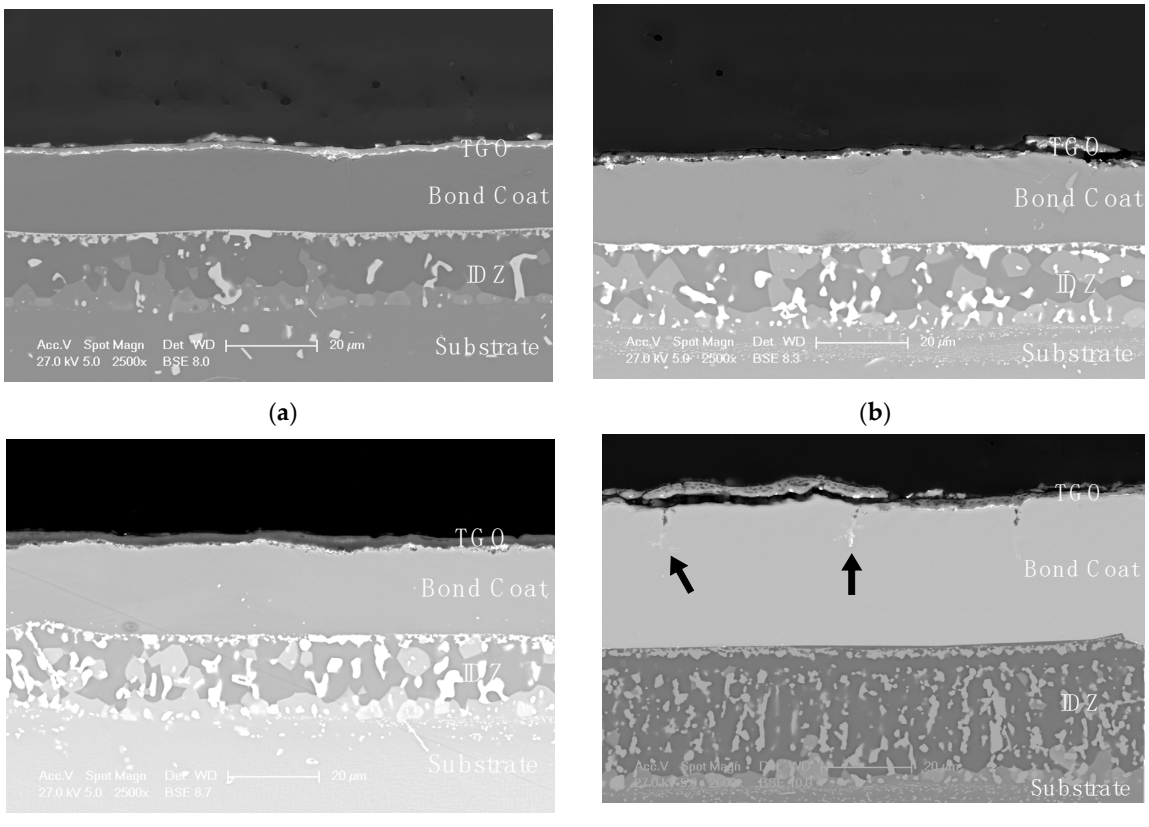

Figure 7. Cross-section SEM micrographs after 100 h oxidation at 1050 °C: (**a**) NF1; (**b**) NF2; (**c**) AlF1; (**d**) AlF2 samples.

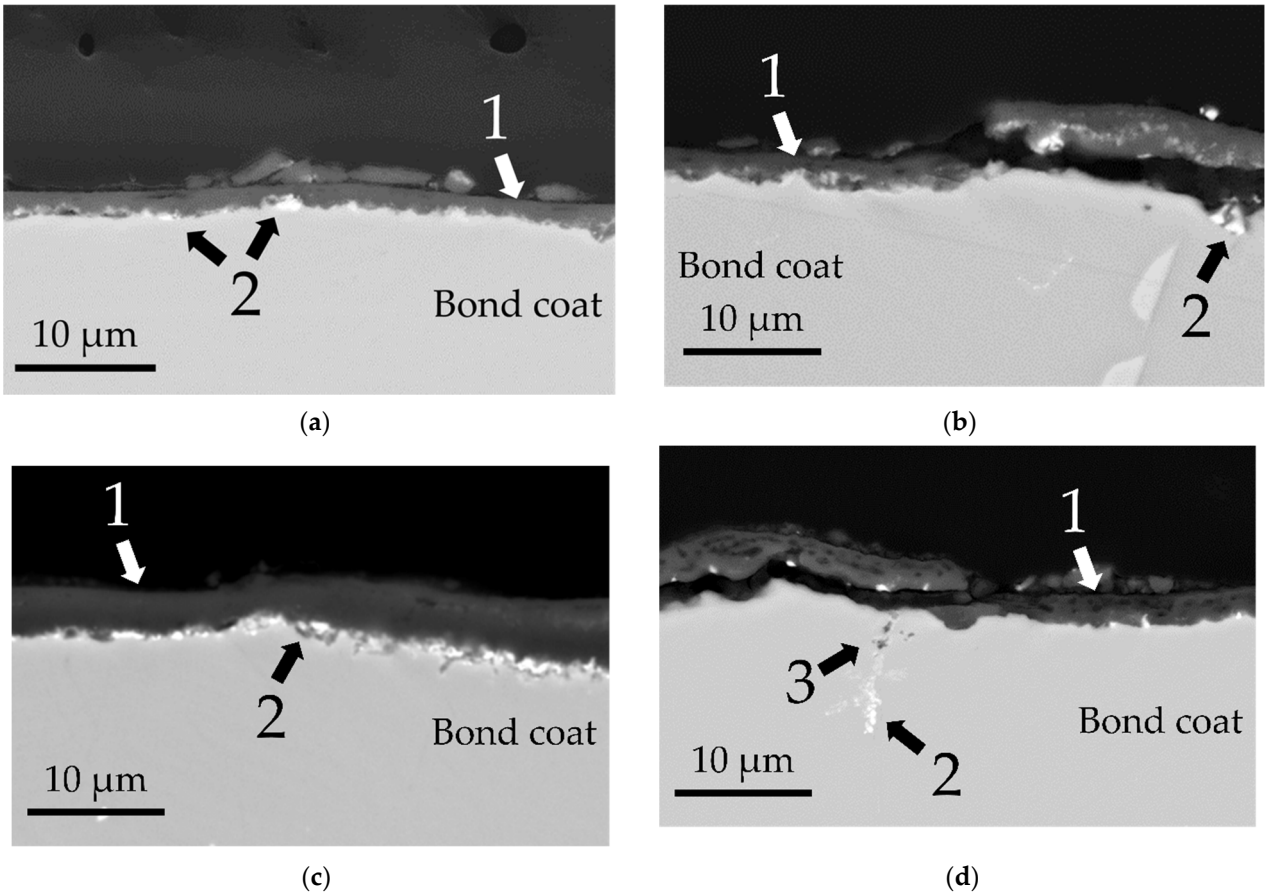

Figure 8. Cross-section SEM micrographs after 100 h oxidation at 1050 °C (detail on the oxide scale): (**a**) NF1; (**b**) NF2; (**c**) AlF1; (**d**) AlF2 samples. In particular, 1 indicates alumina scale (TGO); 2 indicates heavy elements (such as Ta and Hf) diffuse from the superalloy during the heat treatment; 3 indicates intergranular oxidation.

The images (Figure 7) show that all types of samples exhibit microstructural changes in the IDZ layer: the high temperature exposure leads to the growth and coalescence of the precipitates formed in the interdiffusion zone during the aluminization process.

The thickness of the surface alumina layer (TGO—thermally grown oxide) for the four samples is comparable (around 2 μm). The oxide scale of AlF2 sample, however, is less homogeneous and appears porous and permeable. This could be the main reason for the higher weight gain exhibited by AlF2, and for the delay in attaining the oxidation plateau (Figure 5). Furthermore, traces of intergranular oxidation are observed in AlF2 diffusion coating (arrows in Figure 7d and marker 3 in Figure 8d), thus confirming the lower protection ability of its oxide scale. In Figure 8d it is possible to observe the presence of the intergranular oxidation (marker 3) and the presence of heavier elements (such as Ta and Hf, marker 2) diffused from the superalloy.

Samples NF1 and AlF1 are characterized by the formation of an oxide scale adherent, cohesive and continuous (Figure 8a–d, marker 1).

On the basis of the comparison of weight gain kinetics and post-oxidation examination, NF1 sample, while including several defects such as micrometric or sub-micrometric Al_2O_3 aggregates, exhibits the best isothermal oxidation resistance.

The graph shown in Figure 9 illustrates the results of the hot corrosion tests for all the types of samples and for uncoated substrate (the complete plot, up to 200 h exposure, is reported in (Figure 9a); a detailed view, up to 100 h exposure, for coated samples only, is shown in (Figure 9b)). Again, as in the case of oxidation, the uncoated substrate proves unable to resist the aggressive environment, produced in this case by corrosive salts, and a large amount of corrosion products spalled since the early thermal cycles. A standard

deviation of about ±15% was calculated for the weight variation at each exposure time (error bars were not reported in the graph for better readability).

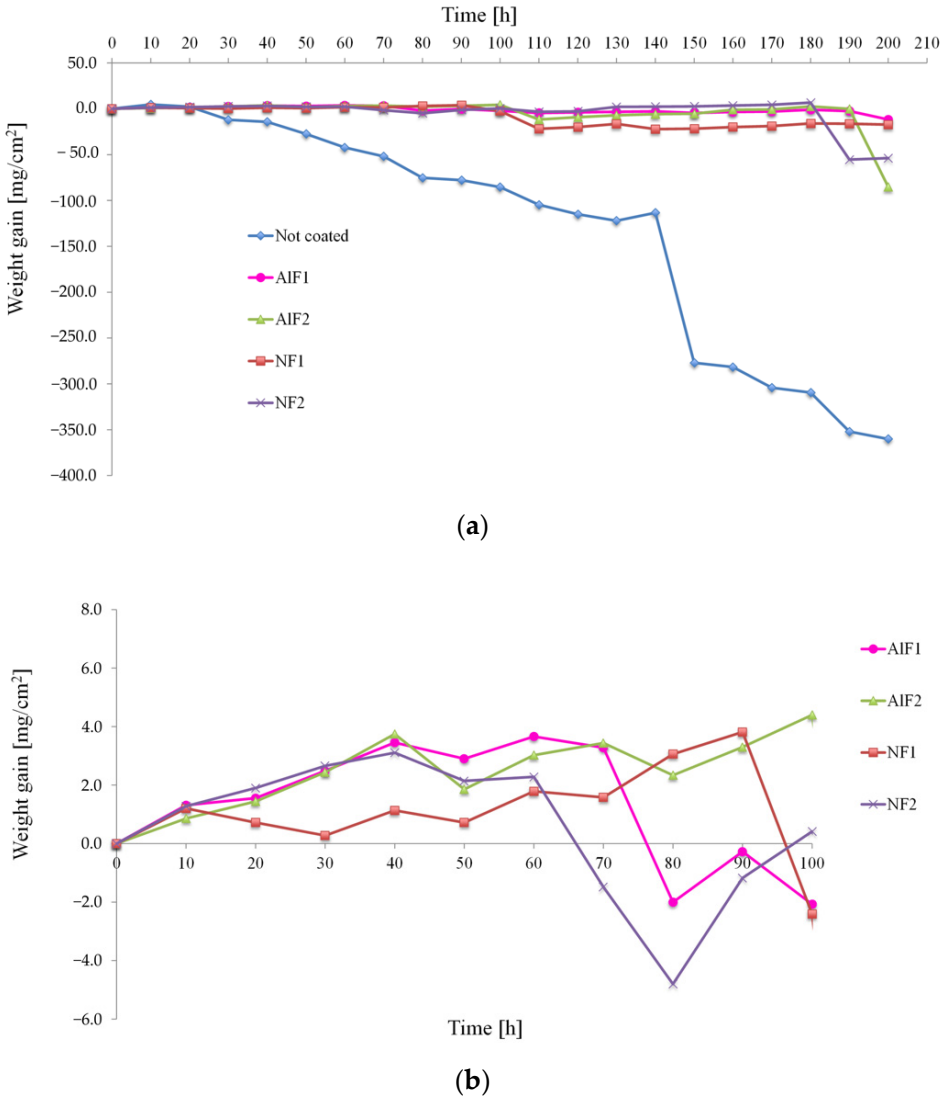

Figure 9. Hot corrosion kinetics (weight gain vs. time) at 900 °C for NF, AlF and not coated samples: (**a**), complete plot, up to 200 h exposure; (**b**) detailed view, up to 100 h exposure, coated samples only.

On the other hand, all coated samples exhibit similar behaviour, demonstrating the positive effect of both NF and AlF diffusion coatings in the protection of the substrate.

By highlighting in more detail the first stage of corrosion (Figure 9b), evident fluctuations in weight change can be observed. This can be explained considering that the test procedure involves a rinse in hot deionized water in between each individual thermal cycle, before evaluating the weight change. This washing procedure certainly eliminates the unreacted salts (NaCl and Na_2SO_4), extremely soluble, but may also be responsible for the mechanical removal of part of the insoluble reaction products that could be weakly adherent to the surface. Such a removal may thus induce a further exposure of the metal surface to corrosive environment.

The cross-section of the NF1 sample after 50, 100, and 150 h of hot corrosion is shown in Figure 10, as a representative example. The corrosion leads to a massive internal oxidation already after 50 h of high temperature exposure. It is possible to see how the oxidation is penetrative for increasing high temperature exposure time as shown in Figure 10b,c, respectively after 100 and 150 h of hot corrosion. Figure 10 also shows the advancing

front of sulfur inside the coating, identified by repeated punctual EDS analyses along an imaginary line starting from the oxide scale and perpendicularly reaching the substrate (Figure 10b,c). Two EDS spectra performed in two different points of the sample are reported in Figure 10d,e. The spectrum in Figure 10d is referred to a point where S was revealed; in contrast, the spectrum reported in Figure 10e shows no trace of S within the instrument's detection limits. In the first 50 h of corrosion, the progress of sulfur inside the coating is null.

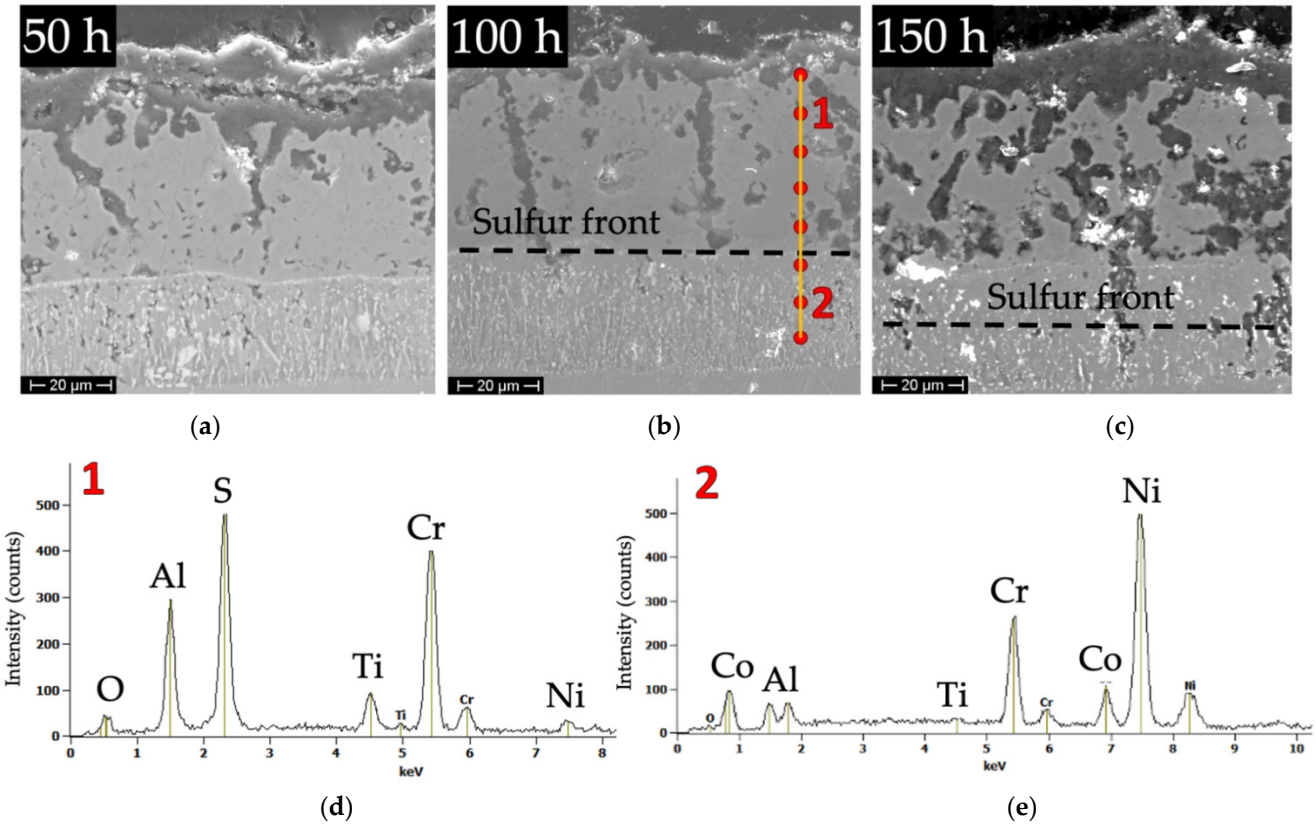

Figure 10. Cross-section SEM images for the hot corrosion test of NF1 sample after: 50 h (**a**), 100 h (**b**) and 150 h (**c**), and EDS spectra for the labelled spots: presence of S (**d**) absence of S (**e**).

It has been demonstrated [40] that once the surface of the metal has been partially or completely wetted by a molten salt deposit, the "type I" hot corrosion mechanism proceeds in two consequent steps: an initiation stage, where a surface oxide is produced, followed by a propagation stage, in which the oxide is dissolved and destroyed, and corrosion rapidly proceeds.

Assuming a similar mechanism is active in the examined case, experimental evidence confirms that in the first 50 h of exposure the process remains in a latent stage of initiation and a surface oxide layer is produced; then, after 50–75 h, the molten salt produces the progressive dissolution of the oxide scale. After the breakdown of the protective scale, sulfur is free to diffuse through the bond coat, attaining the substrate for further increasing high temperature exposure.

As shown in Figure 9, two samples (NF1 and AlF2) begin to lose weight after 180 h and 190 h. As expected, for those samples, the coating is completely corroded after 200 h of exposure, as reported in Figure 11. The dark areas, pointed by arrows, indicate the points where the initial detachment of the coating took place, with extensive loss of material; this phenomenon occurred because, once all the coating (bond coat and IDZ) has been consumed, corrosion has disastrous consequences on the superalloy exposed to the harsh atmosphere.

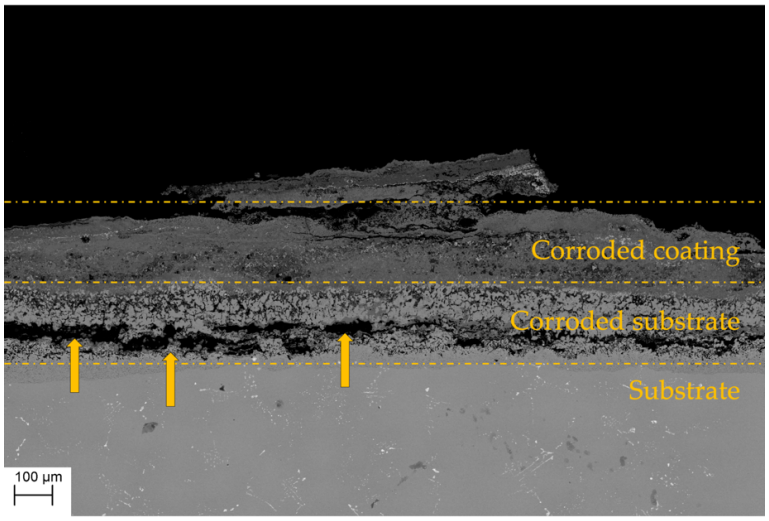

Figure 11. Cross-section SEM images for the hot corrosion test of AlF2 sample after 200 h.

Coatings produced with the higher concentration of AlF (AlF2) exhibit the best hot corrosion resistance. In detail, from the curves of Figure 8b, it appears that the spallation and sudden weight loss of the samples occurs after 60, 70, and 90 h for the samples NF2, AlF1 and NF1 respectively, while it is delayed beyond 100 h for the samples AlF2. The specific hot corrosion resistance of AlF2 samples can be explained by the presence of a thicker β-NiAl coating zone (30 µm, against 20 µm for NF2, as reported in Table 4), allowing for longer exposures to salts. Further discussion of these results is provided in the next sections.

3.3. Comparison of Phase Structure and Microstructure of Coatings after Exposure Tests

3.3.1. Isothermal Oxidation

EDS analysis was performed on the cross-section of the oxidized coatings. Figure 12 shows the elemental map of the NF2 coating after 100 h of oxidation at 1050 °C; the elemental distribution is also representative of the other coatings tested for the same exposure time.

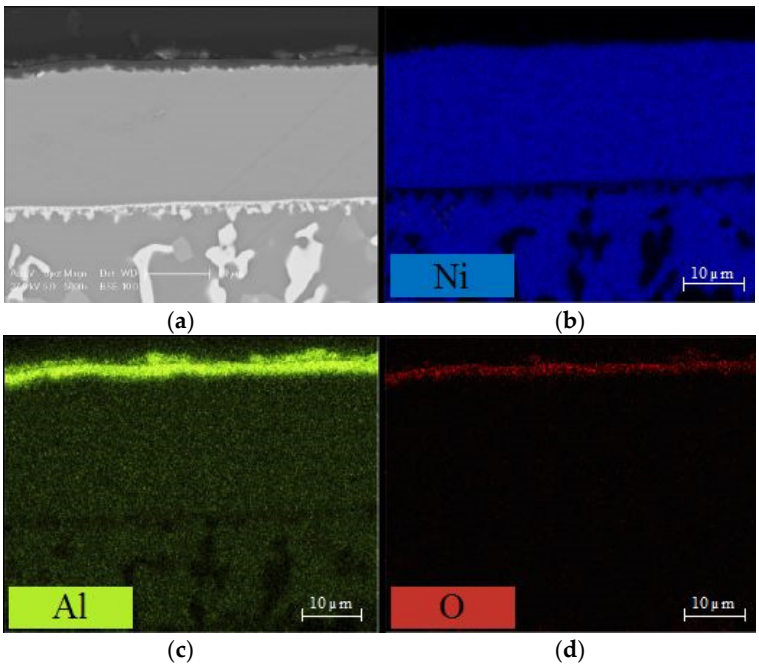

Figure 12. *Cont.*

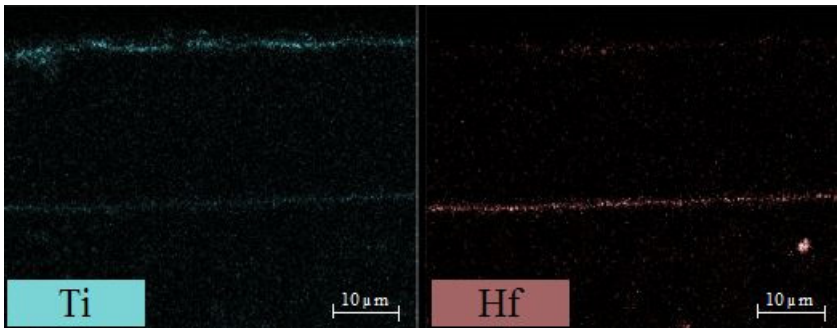

(**e**) (**f**)

Figure 12. EDS maps of sample NF2 after 105 h oxidation at 1050 °C; (**a**) cross-section micrograph and (**b**) Ni, (**c**) Al, (**d**) O, (**e**) Ti, (**f**) Hf elemental maps.

The presence of Al and O was revealed in correspondence with the oxide scale (Figure 12d), confirming the formation of an Al_2O_3—rich layer. The EDS also highlights the presence of Ti and, in much smaller amounts, Hf, immediately below the Al_2O_3 scale (Figure 12e,f) due to the outward diffusion of these two alloy elements from the IDZ towards the β-NiAl diffusion coating.

Figure 13 illustrates the surface phase evolution of NF2 sample, obtained by comparing the XRD patterns after 25, 50, 75 and 100 h of exposure. The analysis confirms the formation of alumina on the top surface, in the form of stable and protective α-Al_2O_3 phase, and shows the presence of Ti and Hf oxides after 50 h of high temperature oxidation, as also reported in the literature [41]. The effect of Ti and other elements composing the superalloy (such as Hf) was studied by Tawancy et al., Bennet et al. and Zhou et al. [31–33]. They demonstrated that low concentration of Ti (<1 wt.%) can be helpful for the oxide scale adherence whereas a higher level of Ti is detrimental to the spallation resistance of the grown oxide.

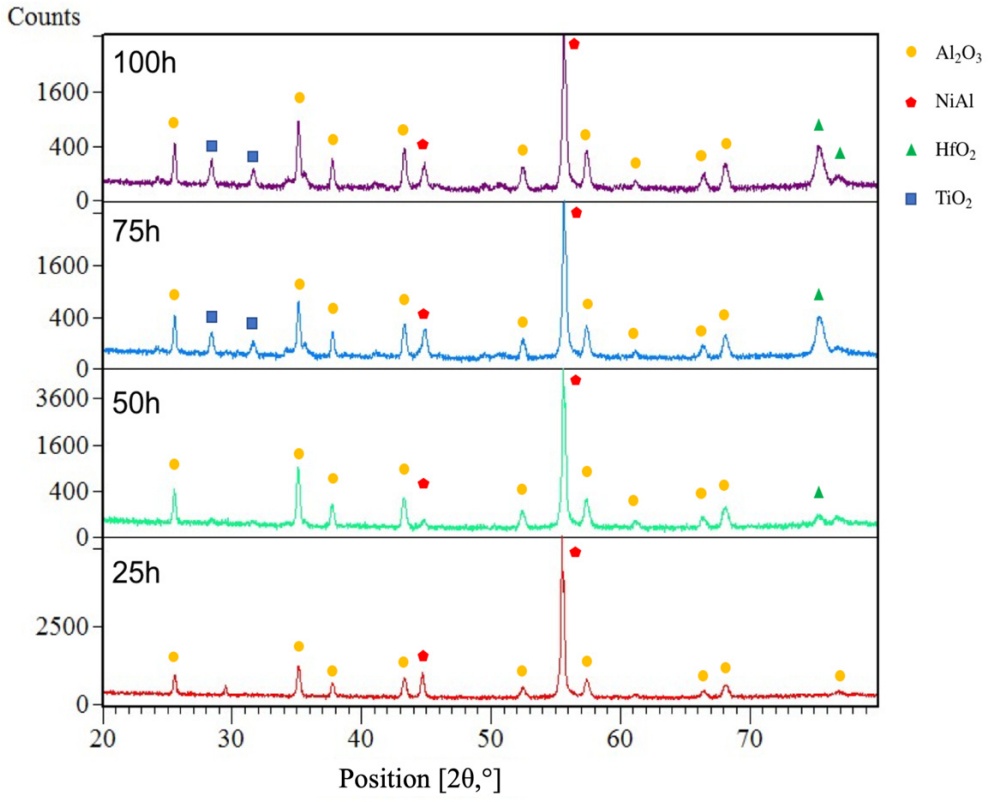

Figure 13. XRD patterns of NF1 sample after 25, 50, 75 and 100 h isothermal oxidation.

The results shown in Section 3.1 about the different formation of the intermetallic depending on the activator salts are confirmed by the analysis of the coating evolution after 100 h of oxidation test: in Figure 14, both the bond coat and the IDZ of AlF2 samples (Figure 14b) exhibit an evident thickness growth after high temperature exposure (right side of the picture). This phenomenon is not observed in the NF sample (Figure 14a): the IDZ microstructure appears modified after the oxidation but without any substantial increase of the thickness.

Qiong Wu et al. [42] demonstrated that in an Al-rich NiAl coating the Al and Ni interdiffusion processes attain an equilibrium state after about 20 h of heat treatment. This means that in the AlF2 samples the increase in the thickness of the NiAl coating and IDZ layer observed after the oxidation test can be attributed to the Al and Ni interdiffusion during the early stages of the high temperature exposure. Therefore, it can be assumed that the selective oxidation mechanism typical of β-NiAl intermetallic was affected by the incomplete diffusion of the Al within the superalloy.

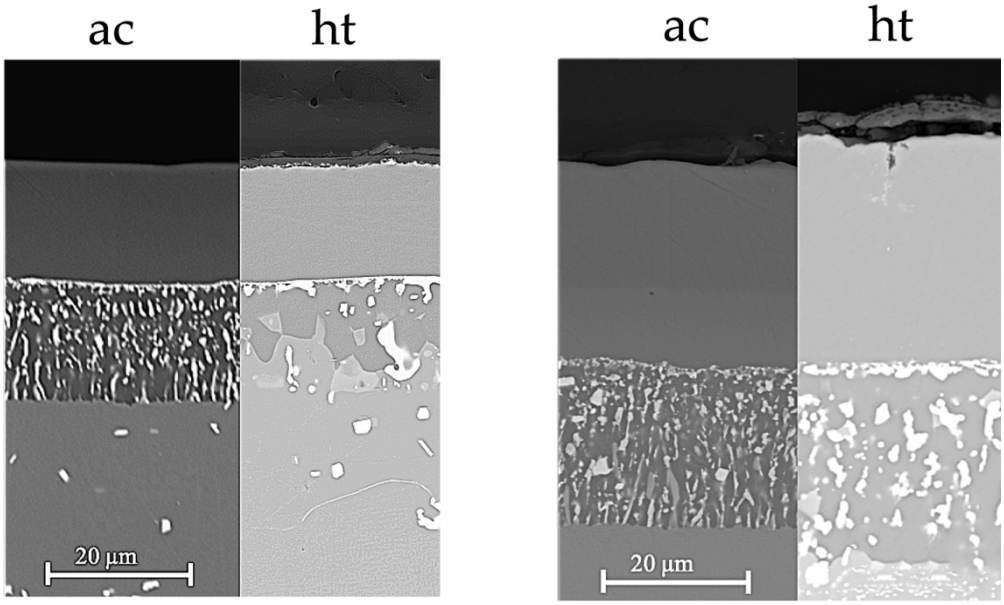

(**a**) (**b**)

Figure 14. Microstructural evolution of the NF1 (**a**) and AlF2 (**b**) samples as-coated (ac) and after 100 h of isothermal oxidation (ht).

3.3.2. Hot Corrosion

Figure 15 shows the cross-section elemental maps of the corroded layer for the NF1 sample after 200 h of hot corrosion test. The analysis reveals the presence of sulphur in the corrosion scale and the XRD results (Figure 16) highlight the presence of NiS_2 in the outer corrosion products.

According to the corrosion mechanisms reported in the literature [21,30,43], the molten salts (melting temperature of about 650 °C) react with the oxide scale continuously dissolving it on the basis of the following reactions:

$$Na_2SO_4 \rightarrow Na_2O + SO_2 + \frac{1}{2} O_2 \quad (4)$$

$$Al_2O_3 + Na_2O \rightarrow AlO_2^- + 2Na^+ \quad (5)$$

$$Al_2O_3 + SO_4^{2-} \rightarrow AlO_2^- + SO_3 \quad (6)$$

Therefore, the corrosion process can be considered as the consequence of two parallel and not independent phenomena:

1. The mechanism of penetration of sulfur within the scale can cause a more aggressive oxidation, also leading to internal corrosion phenomena (as reported in Figure 10).
2. the scale dissolution reaction consumes the protective layer, therefore exposing the metal to further corrosion.

Furthermore, the presence of Cl^- accelerates the process of dissolution of the scale according to the reaction:

$$Al_2O_3 + \frac{1}{2} O_2 + 2NaCl \rightarrow 2NaAlO_2 + Cl_2 \quad (7)$$

The reactions involved in the mechanism lead to the formation of a porous scale that does not provide protection for the underlying metal. For this reason, it can be assumed that in the case of hot corrosion, the thicker bond coat layer obtained in the AlF samples could have a positive influence in terms of hot corrosion resistance for two reason:

1. The thicker bond coat involves a longer path for sulfur to reach the substrate.
2. The outward diffusion of Ni observed during the high temperature exposure in the AlF samples (leading to the further growth of the NiAl layer) could oppose to the sulfur inward diffusion within the bond coat, thus reducing the sulfur (in the form of SO_3) penetration kinetics.

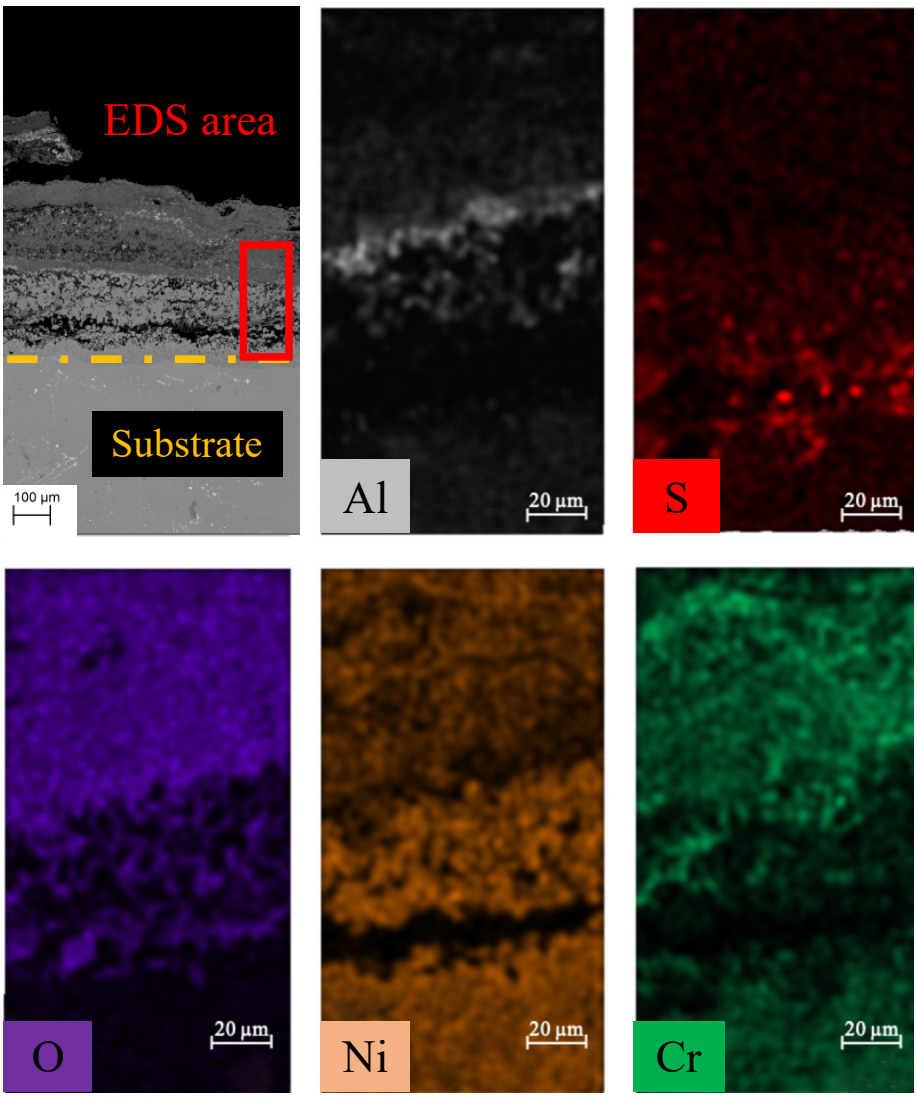

Figure 15. EDS maps of corrosion area for sample NF1 (before washing) after 200 h hot corrosion test at 900 °C.

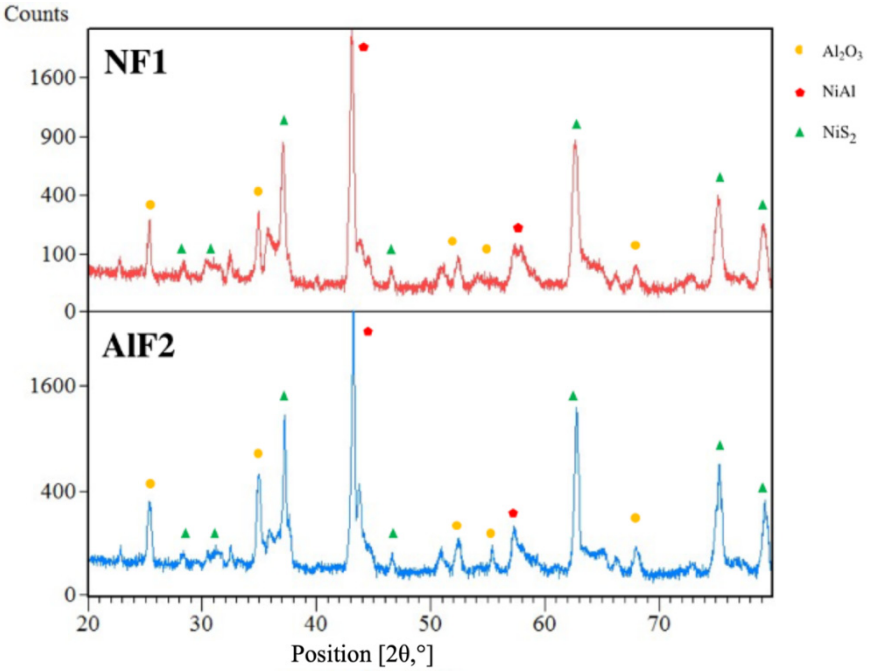

Figure 16. XRD patterns of samples NF1 and AlF2 after 100 h exposure at 900 °C to hot corrosion in the presence of NaCl and Na_2SO_4.

4. Conclusions

The isothermal oxidation and hot corrosion resistance of coatings obtained by HTLA pack cementation using two different activator salts were investigated; the results confirmed that:

- the use of AlF_3 allows the growth of a thicker diffusion coating. Due to the higher concentration in the vapour phase of Al, originating both from the thermal decomposition of the activator salt and from the reaction with the aluminium pack, thicker Al-rich β-NiAl and IDZ layers grow on the Ni-based alloy surface;
- the coatings obtained with NH_4F show a higher resistance to the isothermal oxidation than the coatings produced with AlF_3; on the other hand, coatings obtained using AlF_3 activator show improved hot corrosion resistance after 100 h due to the higher thickness of the β-NiAl coating. This result has been ascribed to the unstable β-NiAl (Al-rich) phase obtained via AlF_3 pack cementation with the higher concentration of activator salt. The high temperature exposure caused a further diffusion of the Al excess present in the outer layer of coatings produced with AlF_3, and this phenomenon is likely to be responsible for the reduced oxidation resistance, as further growth of the NiAl layer probably affects the thermally grown oxide formation mechanisms. At the same time, it was proved to increase the hot corrosion resistance because the outward diffusion of Ni and the thicker NiAl layer may hinder the penetration of sulfur.

Author Contributions: Data curation, V.G. and L.P.; Formal analysis, V.G., G.P. and F.M.; Funding acquisition, G.P. and F.M.; Investigation, V.G., L.P. and F.M.; Resources, F.M.; Supervision, G.P. and C.B.; Validation, C.B.; Writing—original draft, V.G., G.P. and C.B. All authors have read and agreed to the published version of the manuscript.

Funding: This research received no external funding.

Institutional Review Board Statement: Not applicable.

Informed Consent Statement: Not applicable.

Data Availability Statement: Data sharing not applicable.

Conflicts of Interest: The authors declare no conflict of interest.

References

1. Brotzu, A.; Felli, F.; Marra, F.; Pilone, D.; Pulci, G. Mechanical properties of a TiAl-based alloy at room and high temperatures. *Mater. Sci. Technol.* **2018**, *34*, 1847–1853. [CrossRef]
2. Pilone, D.; Pulci, G.; Paglia, L.; Mondal, A.; Marra, F.; Felli, F.; Brotzu, A. Mechanical behaviour of an Al_2O_3 dispersion strengthened γTiAl alloy produced by centrifugal casting. *Metals* **2020**, *10*, 1457. [CrossRef]
3. Beranoagirre, A.; Urbikain, G.; Calleja, A.; de Lacalle, L.N.L. Drilling process in γ-TiAl intermetallic alloys. *Materials* **2018**, *11*, 2379. [CrossRef]
4. Boissonnet, G.; Grégoire, B.; Bonnet, G.; Pedraza, F. Development of thermal barrier coating systems from Al microparticles. Part I: Influence of processing conditions on the mechanisms of formation. *Surf. Coat. Technol.* **2019**, *380*, 125085. [CrossRef]
5. Grégoire, B.; Bonnet, G.; Pedraza, F. Development of a new slurry coating design for the surface protection of gas turbine components. *Surf. Coat. Technol.* **2019**, *374*, 521–530. [CrossRef]
6. Pedraza, F.; Mollard, M.; Rannou, B.; Balmain, J.; Bouchaud, B.; Bonnet, G. Potential thermal barrier coating systems from Al microparticles. Mechanisms of coating formation on pure nickel. *Mater. Chem. Phys.* **2012**, *134*, 700–705. [CrossRef]
7. Baiamonte, L.; Marra, F.; Pulci, G.; Tirillò, J.; Sarasini, F.; Bartuli, C.; Valente, T. High temperature mechanical characterization of plasma-sprayed zirconia-yttria from conventional and nanostructured powders. *Surf. Coat. Technol.* **2015**, *277*, 289–298. [CrossRef]
8. Di Girolamo, G.; Marra, F.; Blasi, C.; Schioppa, M.; Pulci, G.; Serra, E.; Valente, T. High-temperature mechanical behavior of plasma sprayed lanthanum zirconate coatings. *Ceram. Int.* **2014**, *40*, 11433–11436. [CrossRef]
9. Pulci, G.; Tirillò, J.; Marra, F.; Sarasini, F.; Bellucci, A.; Valente, T.; Bartuli, C. High temperature oxidation and microstructural evolution of modified *M*CrAlY coatings. *Met. Mater. Trans. A Phys. Met. Mater. Sci.* **2014**, *45*, 1401–1408. [CrossRef]
10. Pomeroy, M.J. Coatings for gas turbine materials and long term stability issues. *Mater. Des.* **2005**, *26*, 223–231. [CrossRef]
11. Di Girolamo, G.; Marra, F.; Schioppa, M.; Blasi, C.; Pulci, G.; Valente, T. Evolution of microstructural and mechanical properties of lanthanum zirconate thermal barrier coatings at high temperature. *Surf. Coat. Technol.* **2015**, *268*, 298–302. [CrossRef]
12. Pulci, G.; Tirillò, J.; Marra, F.; Sarasini, F.; Bellucci, A.; Valente, T.; Bartuli, C. High temperature oxidation of *M*CrAlY coatings modified by Al_2O_3 PVD overlay. *Surf. Coat. Technol.* **2015**, *268*, 198–204. [CrossRef]
13. Zagula-Yavorska, M.; Romanowska, J.; Sieniawski, J.; Wierzbińska, M. Hafnium modified aluminide coatings obtained by the CVD and PVD methods. *Solid State Phenom.* **2015**, *227*, 353–356. [CrossRef]
14. Warnes, B.M. Improved aluminide/MCrAlX coating systems for super alloys using CVD low activity aluminizing. *Surf. Coat. Technol.* **2003**, *163*, 106–111. [CrossRef]
15. Voudouris, N.; Christoglou, C.; Angelopoulos, G.N. Formation of aluminide coatings on nickel by a fluidised bed CVD process. *Surf. Coat. Technol.* **2001**, *141*, 275–282. [CrossRef]
16. Levine, S.R.; Caves, R.M. Thermodynamics and kinetics of pack aluminide coating formation on IN-100. *J. Electrochem. Soc.* **1974**, *121*, 1051. [CrossRef]
17. Rakov, E.G.; Mel'nichenko, E.I. The properties and reactions of ammonium fluorides. *Russ. Chem. Rev.* **1984**, *53*, 851–869. [CrossRef]
18. Menz, D.-H.; Zacharias, A.; Kolditz, L. A comparison of the thermal behaviour of α-AlF_3 and aluminium fluoride hydrates. *J. Therm. Anal. Calorim.* **1988**, *33*, 811–815. [CrossRef]
19. Nowak, W.J.; Ochał, K.; Wierzba, P.; Gancarczyk, K.; Wierzba, B. Effect of substrate roughness on oxidation resistance of an aluminized Ni-base superalloy. *Metals* **2019**, *9*, 782. [CrossRef]
20. Bozza, F.; Bolelli, G.; Giolli, C.; Giorgetti, A.; Lusvarghi, L.; Sassatelli, P.; Scrivani, A.; Candeli, A.; Thoma, M. Diffusion mechanisms and microstructure development in pack aluminizing of Ni-based alloys. *Surf. Coat. Technol.* **2014**, *239*, 147–159. [CrossRef]
21. Lu, J.; Zhu, S.; Wang, F. Cyclic oxidation and hot corrosion behavior of Y/Cr-modified aluminide coatings prepared by a hybrid slurry/pack cementation process. *Oxid. Met.* **2011**, *76*, 67–82. [CrossRef]
22. Warnes, B.M.; Punola, D.C. Clean diffusion coatings by chemical vapor deposition. *Surf. Coat. Technol.* **1997**, *94*, 1–6. [CrossRef]
23. Goward, G.W.; Boone, D.H. Mechanisms of formation of diffusion aluminide coatings on nickel-base superalloys. *Oxid. Met.* **1971**, *3*, 475–495. [CrossRef]
24. Yang, Y.F.; Jiang, C.Y.; Bao, Z.B.; Zhu, S.L.; Wang, F.H. Effect of aluminisation characteristics on the microstructure of single phase β-(Ni,Pt)Al coating and the isothermal oxidation behaviour. *Corros. Sci.* **2016**, *106*, 43–54. [CrossRef]
25. Warnes, B.M. Reactive element modified chemical vapor deposition low activity platinum aluminide coatings. *Surf. Coat. Technol.* **2001**, *146*, 7–12. [CrossRef]
26. Xiang, Z.D.; Burnell-Gray, J.S.; Datta, P.K. Aluminide coating formation on nickel-base superalloys by pack cementation process. *J. Mater. Sci.* **2001**, *36*, 5673–5682. [CrossRef]
27. Naveos, S.; Oberlaender, G.; Cadoret, Y.; Josso, P.; Bacos, M.P. Zirconium modified aluminide by a vapour pack cementation process for thermal barrier applications: Formation mechanisms and properties. *Mater. Sci. Forum.* **2004**, *461*, 375–382. [CrossRef]
28. Baiamonte, L.; Marra, F.; Gazzola, S.; Giovanetto, P.; Bartuli, C.; Valente, T.; Pulci, G. Thermal sprayed coatings for hot corrosion protection of exhaust valves in naval diesel engines. *Surf. Coat. Technol.* **2016**, *295*, 78–87. [CrossRef]
29. Chatha, S.S.; Sidhu, H.S.; Sidhu, B.S. High temperature hot corrosion behaviour of NiCr and Cr_3C_2-NiCr coatings on T91 boiler steel in an aggressive environment at 750 °C. *Surf. Coat. Technol.* **2012**, *206*, 3839–3850. [CrossRef]

30. Li, C.; Xu, X.; Wang, S.; Tabie, V.M.; Yang, S.; Zhang, T.; Liu, Y. High-temperature oxidation and hot corrosion behavior of the Cr-modified aluminide coating obtained by a thermal diffusion process. *Mater. Res. Express.* **2019**, *6*, 086444. [CrossRef]
31. Zhang, K.; Liu, M.M.; Liu, S.L.; Sun, C.; Wang, F.H. Hot corrosion behaviour of a cobalt-base super-alloy K40S with and without NiCrAlYSi coating. *Corros. Sci.* **2011**, *53*, 1990–1998. [CrossRef]
32. Tolpygo, V.K.; Clarke, D.R. Rumpling of CVD (Ni,Pt)Al diffusion coatings under intermediate temperature cycling. *Surf. Coat. Technol.* **2009**, *203*, 3278–3285. [CrossRef]
33. Zielińska, M.; Zagula-Yavorska, M.; Sieniawski, J.; Filip, R. Microstructure and oxidation resistance of an aluminide coating on the nickel based superalloy Mar M247 deposited by the CVD aluminizing process. *Arch. Met. Mater.* **2013**, *58*, 697–701. [CrossRef]
34. Xiang, Z.D.; Datta, P.K. Pack cementation process for the formation of refractory metal modified aluminide coatings on nickel-base superalloys. *J. Mater. Sci.* **2003**, *38*, 3721–3728. [CrossRef]
35. Bianco, R.; Rapp, R.A. Pack cementation diffusion coatings. In *Metallurgical and Ceramic Protective Coatings*; Stern, K.H., Ed.; Springer: Berlin/Heidelberg, Germany, 1996; pp. 236–260.
36. Yamai, I.; Saito, H. Vapor phase growth of alumina whiskers by hydrolysis of aluminum fluoride. *J. Cryst. Growth* **1978**, *45*, 511–516. [CrossRef]
37. Riello, D.; Zetterström, C.; Parr, C.; Braulio MA, L.; Moreira, M.; Gallo, J.B.; Pandolfelli, V.C. AlF_3 reaction mechanism and its influence on α-Al_2O_3 mineralization. *Ceram. Int.* **2016**, *42*, 9804–9814. [CrossRef]
38. Monceau, D.; Pieraggi, B. Determination of parabolic rate constants from a local analysis of mass-gain curves. *Oxid. Met.* **1998**, *50*, 477–493. [CrossRef]
39. Taylor, A.; Doyle, N.J. Further studies on the nickel–aluminium system. I. β-NiAl and δ-Ni_2Al_3 phase fields. *J. Appl. Cryst.* **1972**, *5*, 201–209. [CrossRef]
40. Prakash, S. Hot corrosion of alloys and coatings. In *Developments in High Temperature Corrosion and Protection of Materials*; Woodhead Publishing: Cambridge, UK, 2008; pp. 164–191. [CrossRef]
41. Liu, G.; Li, M.; Zhu, M.; Zhou, Y. Transient of alumina oxide scale on β-NiAl coated on M38G alloy at 950 °C. *Intermetallics* **2007**, *15*, 1285–1290. [CrossRef]
42. Wu, Q.; Li, S.; Ma, Y.; Gong, S. Study on behavior of NiAl coating with different Ni/Al ratios. *Vaccum* **2013**, *93*, 37–44. [CrossRef]
43. Fan, Q.X.; Jiang, S.M.; Wu, D.L.; Gong, J.; Sun, C. Preparation and hot corrosion behaviour of two Co modified NiAl coatings on a Ni-based superalloy. *Corros. Sci.* **2013**, *76*, 373–381. [CrossRef]